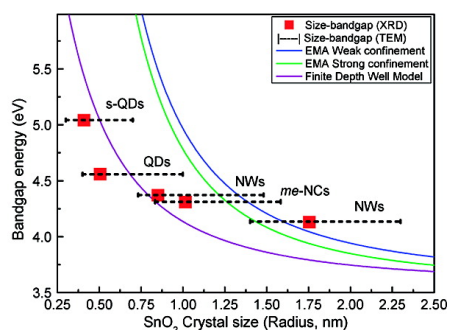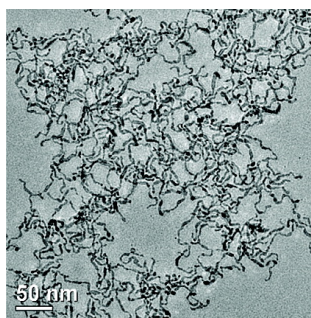Article

SnO Quantum Dots and Quantum Wires: Controllable Synthesis, Self-Assembled 2D Architectures, and Gas-Sensing Properties

Xiangxing Xu, Jing Zhuang, and Xun Wang

More About This Article

Additional resources and features associated with this article are available within the HTML version:

- Supporting Information
- Access to high resolution figures
- Links to articles and content related to this article
- Copyright permission to reproduce figures and/or text from this article

View the Full Text HTML

SnO₂ Quantum Dots and Quantum Wires: Controllable Synthesis, Self-Assembled 2D Architectures, and Gas-Sensing Properties

Xiangxing Xu, Jing Zhuang, and Xun Wang*

Department of Chemistry, Tsinghua University, Beijing 100084, P. R. China

Received June 4, 2008; E-mail: wangxun@mail.tsinghua.edu.cn

Abstract: SnO_2 quantum dots (QDs) and ultrathin nanowires (NWs) with diameters of ~0.5−2.5 and ~1.5−4.5 nm, respectively, were controllably synthesized in a simple solution system. They are supposed to be ideal models for studying the continuous evolution of the quantum-confinement effect in SnO_2 1D → 0D systems. The observed transition from strong to weak quantum confinement in SnO_2 QDs and ultrathin NWs is interpreted through the use of the Brus effective-mass approximation and the Nosaka finite-depth well model. Photoluminescence properties that were coinfluenced by size effects, defects (oxygen vacancies), and surface capping are discussed in detail. With the SnO_2 QDs as building blocks, various 2D porous structures with ordered hexagonal, distorted hexagonal, and square patterns were prepared on silicon-wafer surfaces and exhibited optical features of 2D photonic crystals and enhanced gas sensitivity.

Introduction

Since the discovery of the quantum-confinement effect in semiconductor nanomaterials, particular interest has been focused on synthesizing semiconductor nanocrystals (NCs) exhibiting a gradual reduction from higher to lower dimensionalities while keeping a constant composition and surface state.[1] In comparison with many reports on zero-dimensional (0D) and one-dimensional (1D) systems,[2] only a few types of materials (CdSe,[3] InP,[4] CdTe,[5] and InAs[6]) have revealed a continuous evolution of the quantum-confinement effect in a 1D → 0D system. Because SnO_2 is an important intrinsically n-type oxide semiconductor with a wide band gap (E_g = 3.6 eV at 300 K), SnO_2 nanoparticles, nanoribbons, nanobelts, and nanowires (NWs) have been prepared by various techniques, such as solution synthesis, vapor-phase growth (e.g., thermal evaporation, molecule-based chemical vapor deposition, and laser ablation), sol−gel methods, and electrospinning.[7] However, no research revealing the continuous evolution of the quantum-confinement effect in 1D → 0D SnO_2 systems has been reported to date. The reason for this is that although SnO_2 NCs showing size effects can be synthesized,[7g,8] SnO_2 NWs always have relatively overgrown radii far larger than the exciton Bohr radius of SnO_2 (2.7 nm). Herein, we report the controllable synthesis of SnO_2 quantum dots (QDs) and ultrathin NWs with diameters of ~0.5−2.5 and ~1.5−4.5 nm, respectively. They are supposed to be ideal models to study SnO_2 0D and 1D quantum systems.

Design of the functionality of the capping ligand on the nanocrystal has long been an intensive interdisciplinary research field. Along with quantum effects, surface effects attain greater significance when the nanocrystal size is decreased to several nanometers because of the resulting rapid increase of the surface-atom ratio. Nanocrystals prepared in a solvent system always have the surface covered with ligands or molecular groups, which commonly favors their solubility in polar or nonpolar solvents. Meanwhile, the capping ligands together with the surface defects modify the energy and lattice structure of the nanocrystal, changing its physical or chemical properties. Our results show that the photoluminescence (PL) spectra of SnO_2 QDs and NWs can be well-tuned via ligand exchange.

(1) (a) Henglein, A. *Chem. Rev.* **1989**, *89*, 1861–1873. (b) Brus, L. E. *Appl. Phys. A: Mater. Sci. Process.* **1991**, *53*, 465–474. (c) Alivisatos, A. P. *Science* **1996**, *271*, 933–937.

(2) (a) Murray, C. B.; Norris, D. J.; Bawendi, M. G. *J. Am. Chem. Soc.* **1993**, *115*, 8706–8715. (b) Duan, X. F.; Lieber, C. M. *Adv. Mater.* **2000**, *12*, 298–302. (c) Peng, Z. A.; Peng, X. G. *J. Am. Chem. Soc.* **2002**, *124*, 3343–3353. (d) Xia, Y. N.; Yang, P. D.; Sun, Y. G.; Wu, Y. Y.; Mayers, B.; Gates, B.; Yin, Y. D.; Kim, F.; Yan, Y. Q. *Adv. Mater.* **2003**, *15*, 353–389. (e) Park, J.; An, K.; Hwang, Y.; Park, J. G.; Noh, H. J.; Kim, J. Y.; Park, J. H.; Hwang, N. M.; Hyeon, T. *Nat. Mater.* **2004**, *3*, 891–895. (f) Wang, X.; Zhuang, J.; Peng, Q. Y.; Li, D. *Nature* **2005**, *437*, 121–124. (g) Cademartiri, L.; Montanari, E.; Calestani, G.; Migliori, A.; Guagliardi, A.; Ozin, G. A. *J. Am. Chem. Soc.* **2006**, *128*, 10337–10346. (h) Kovalenko, M. V.; Heiss, W.; Shevchenko, E. V.; Lee, J. S.; Schwinghammer, H.; Alivisatos, A. P.; Talapin, D. V. *J. Am. Chem. Soc.* **2007**, *129*, 11354–11355.

(3) Yu, H.; Li, J.; Loomis, R. A.; Gibbons, P. C.; Wang, L. W.; Buhro, W. E. *J. Am. Chem. Soc.* **2003**, *125*, 16168–16169.

(4) Yu, H.; Li, J.; Loomis, R. A.; Wang, L. W.; Buhro, W. E. *Nat. Mater.* **2003**, *2*, 517–520.

(5) Tang, Z.; Kotov, N. A.; Giersig, M. *Science* **2002**, *297*, 237–240.

(6) Kan, S.; Mokari, T.; Rothenberg, E.; Banin, U. *Nat. Mater.* **2003**, *2*, 155–158.

(7) (a) Wang, Y. L.; Jiang, X. C.; Xia, Y. N. *J. Am. Chem. Soc.* **2003**, *125*, 16176–16177. (b) Zhang, D. F.; Sun, L. D.; Yin, J. L.; Yan, C. H. *Adv. Mater.* **2003**, *15*, 1022–1025. (c) Pan, Z. W.; Dai, Z. R.; Wang, Z. L. *Science* **2001**, *291*, 1947–1949. (d) Mathur, S.; Barth, S. *Small* **2007**, *3*, 2070–2075. (e) Kuang, Q.; Lao, C. S.; Wang, Z. L.; Xie, Z. X.; Zheng, L. S. *J. Am. Chem. Soc.* **2007**, *129*, 6070–6071. (f) Liu, Z.; Zhang, D.; Han, S.; Li, C.; Tang, T.; Jin, W.; Liu, X.; Zhou, C. *Adv. Mater.* **2003**, *15*, 1754–1757. (g) Pang, G. S.; Chen, S. G.; Koltypin, Y.; Zaban, A.; Peng, S. H.; Gedanken, A. *Nano Lett.* **2001**, *1*, 723–726. (h) Kolmakov, A.; Zhang, Y.; Cheng, G.; Moskovits, M. *Adv. Mater.* **2003**, *15*, 997–1000. (i) Li, D.; Wang, Y. L.; Xia, Y. N. *Adv. Mater.* **2004**, *16*, 361–366.

(8) Lee, E. J. H.; Ribeiro, C.; Giraldi, T. R.; Longo, E.; Leite, E. R.; Varela, J. A. *Appl. Phys. Lett.* **2004**, *84*, 1745–1747.

Tailored SnO_2 surface structure and increased effective Brunauer−Emmet−Teller (BET) surface area are essential features for many applications, such as transparent conductors, field emissions, field-effect transistors, solar cells, rechargeable Li batteries, oxidation catalysis, and chemical gas sensing.[7,9] For nanocrystals synthesized in solution systems, the solvent-removal procedures (e.g., simple evaporation) often lead to significant densification and loss of porosity of the material. Therefore, strict control the aggregation or assembly states of SnO_2 is required. Using a block copolymer template is one of the strategies for preparing SnO_2 mesoporous structures.[10] Recently, we reported a novel self-assembly method combining both self-assembled nanocrystal superlattices and water-droplet self-assembled patterns that can be used to generate various combinatorial hierarchical porous architectures with nanocrystals as building blocks.[11] In this article, we demonstrate that the same self-assembly strategy also provides a competitive approach for generating a variety of porous structures using as-prepared SnO_2 QDs as building blocks. In this regard, various 2D porous structures of ordered hexagonal, distorted hexagonal, and square patterns were prepared on silicon-wafer surface by controlling the humidity flow and solution concentration. Optical features of 2D photonic crystals were examined in those patterned SnO_2 QD films. In comparison with smooth films of SnO_2 QDs and ultrathin NWs, a magnificent improvement of the gas sensitivity was achieved.

Experimental Section

Synthesis and Characterization. The synthesis system includes tin(IV) chloride pentahydrate ($SnCl_4 \cdot 5H_2O$), oleic acid (OA), oleylamine (80−90% C18 content, Acros), and various alcohols (methanol, ethanol, ethanediol, or hexanol, etc.). All of the chemicals were used as received without further purification. The Sn−OA precursor was simply prepared by dissolving $SnCl_4 \cdot 5H_2O$ in OA and heating for 1 h under a N_2 gas flow, after which the product was precipitated by adding enough ethanol, centrifuged, and dried at 70 °C in air. In a typical synthesis of SnO_2 QDs and ultrathin NWs, 1.7 mmol $SnCl_4 \cdot 5H_2O$ was dissolved in a mixed solvent of 20 mL OA and 2.5 mL oleylamine by heating to form a clear solution. Next, 10 mL of ethanol was added, and the whole solution was transferred into a Teflon-lined stainless-steel autoclave to react at 180 °C. The reaction time was varied from 30 min to 18 h. The products were separated by adding 40 mL of ethanol and centrifuging at 10 000 rpm for 10 min. The precipitate was washed twice by redispersion in cyclohexane, addition of ethanol, and centrifugation. The final product was dispersed in chloroform. Solid samples were obtained by air-drying at 70 °C. SnO_2 nanocrystals were also prepared by substituting ethanol for methanol (180 °C, 18 h); nanocrystals prepared using methanol are called "*me*-NCs" in this paper, while SnO_2 nanomaterials without the "*me*" prefix are understood to be prepared using the ethanol-containing system.

Characterization. The phase purity of the products was verified by powder X-ray diffraction (XRD) on a Bruker D8 Advance X-ray
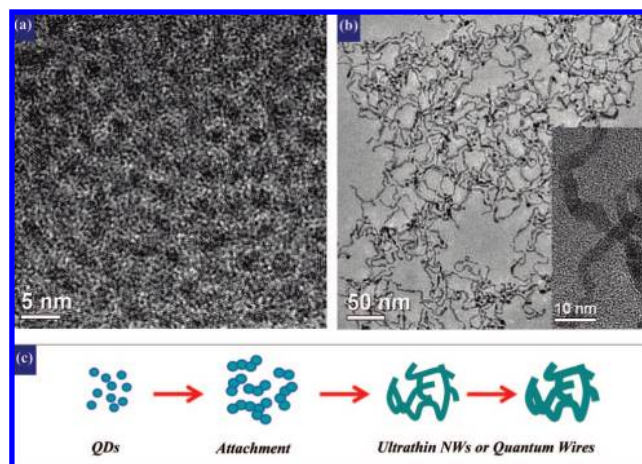

Figure 1. TEM/HRTEM images of SnO_2 (a) QDs and (b) ultrathin NWs. (c) Schematic illustration of the evolution of the SnO_2 morphology from QDs to NWs.

diffractometer using Cu Kα radiation ($\lambda = 1.5418$ Å). The sizes and morphologies of the nanocrystals and films were measured using a JEOL JEM-1200EX transmission electron microscope (TEM) at 120 kV, a Tecnai G2 F20 S-Twin high-resolution transmission electron microscope (HRTEM) at 200 kV, and a JEOL JSM-6700F scanning electron microscope (SEM) at 10 kV. UV−vis absorption spectra were measured on a Hitachi U-3010 spectrophotometer. PL spectra were recorded with a Hitachi F-4500 fluorescence spectrophotometer. FT-IR spectroscopy was performed using a Nicolet 560 spectrograph.

2D Pattern Preparation. A chloroform solution containing SnO_2 or SnO_2−Ag (60 mg mL^{-1}) was dropped onto a quartz- or silicon-wafer surface, and then the solvent was evaporated while a carrier gas (N_2−H_2O) with a controlled flow rate and relative humidity (RH) of 50−98% was flowing over the surface at room temperature (10−20 °C). A flowmeter was used to tune the flow rate. The as-assembled patterns were investigated by SEM and UV−vis spectrophotometry.

Gas-Sensing Measurements. The gas-sensing measurement system used is described in detail elsewhere.[12] Briefly, the nanocrystal solution was dropped onto a ceramic tube on which a pair of Au electrodes were already printed. A flow of carrier gas (N_2−H_2O) was maintained over the surface to prepare self-assembled porous films. In the test process, the resistance response of the sensor for the test gas was measured by monitoring the voltage across the load resistor.

Results and Discussion

Structure and Morphology. TEM images illustrate the evolution of the morphology from SnO_2 QDs to ultrathin NWs over time (Figure 1). At the primary stage, small-sized SnO_2 QDs (*s*-QDs) were incubated within 30 min of the reaction (Figure SI-1 in the Supporting Information); medium reaction times (1−2 h) yielded bigger QDs, and long reaction times (4−18 h) formed twisted and branched NWs with increased diameters of 1.7−3.5 nm (as determined by XRD). The SnO_2 *me*-NCs had irregular shapes and random aggregates (Figure SI-2 in the Supporting Information). XRD measurements (Figure 2a) showed that the products were SnO_2 with a pure tetragonal phase having the rutile structure (JCPDS 88−0287). The gradual widening of the peaks from NWs to QDs indicates the decrease

(9) (a) Peng, Z. Y.; Shi, Z.; Liu, M. L. *Chem. Commun.* **2000**, 2125–2126. (b) Dattoli, E. N.; Wan, Q.; Guo, W.; Chen, Y. B.; Pan, X. Q.; Lu, W. *Nano Lett.* **2007**, *7*, 2463–2469. (c) Cheng, Y.; Xiong, P.; Fields, L.; Zheng, J. P.; Yang, R. S.; Wang, Z. L. *Appl. Phys. Lett.* **2006**, *89*, 093114. (d) Chappel, S.; Chen, S. G.; Zaban, A. *Langmuir* **2002**, *18*, 3336–3342. (e) Zhao, Q. R.; Zhang, Z. G.; Dong, T.; Xie, Y. *J. Phys. Chem. B* **2006**, *110*, 15152–15156. (f) Ying, Z.; Wan, Q.; Cao, H.; Song, Z. T.; Feng, S. L. *Appl. Phys. Lett.* **2005**, *87*, 113108.

(10) (a) Ba, J. H.; Polleux, J.; Antonietti, M.; Niederberger, M. *Adv. Mater.* **2005**, *17*, 2509–2512. (b) Tiemann, M. *Chem.—Eur. J.* **2007**, *13*, 8377–8388.

(11) Xu, X. X.; Wang, X.; Nisar, A.; Liang, X.; Zhuang, J.; Hu, S.; Zhuang, Y. *Adv. Mater.* **2008**, in press.

(12) Zhuang, Z. B.; Peng, Q.; Liu, J. F.; Wang, X.; Li., Y. D. *Inorg. Chem.* **2007**, *46*, 5179–5187.
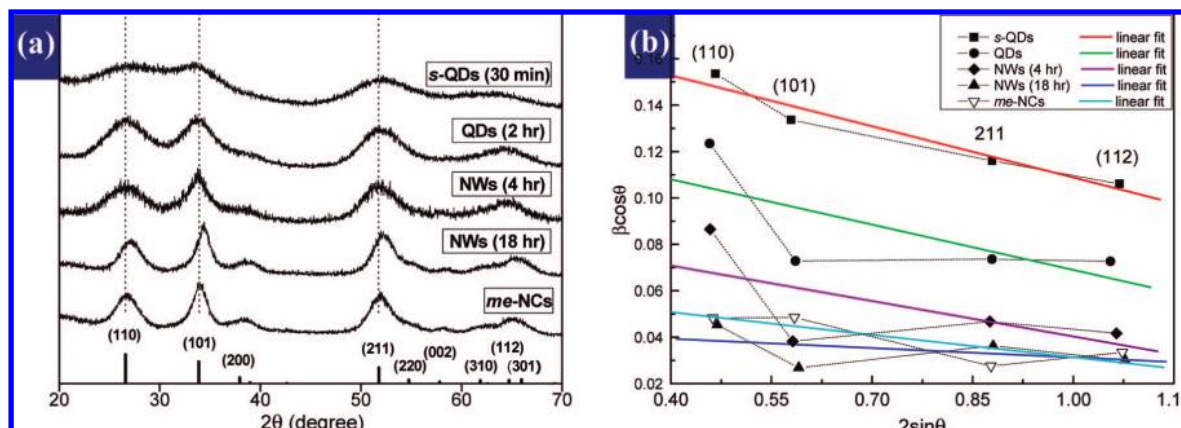
Figure 2. (a) XRD patterns of SnO₂ QDs, NWs, and *me*-NCs; the JCPDS 88−0287 diffraction pattern is shown at the bottom. (b) Plots of measured XRD data and corresponding linear fits using eqs 1 and 2.
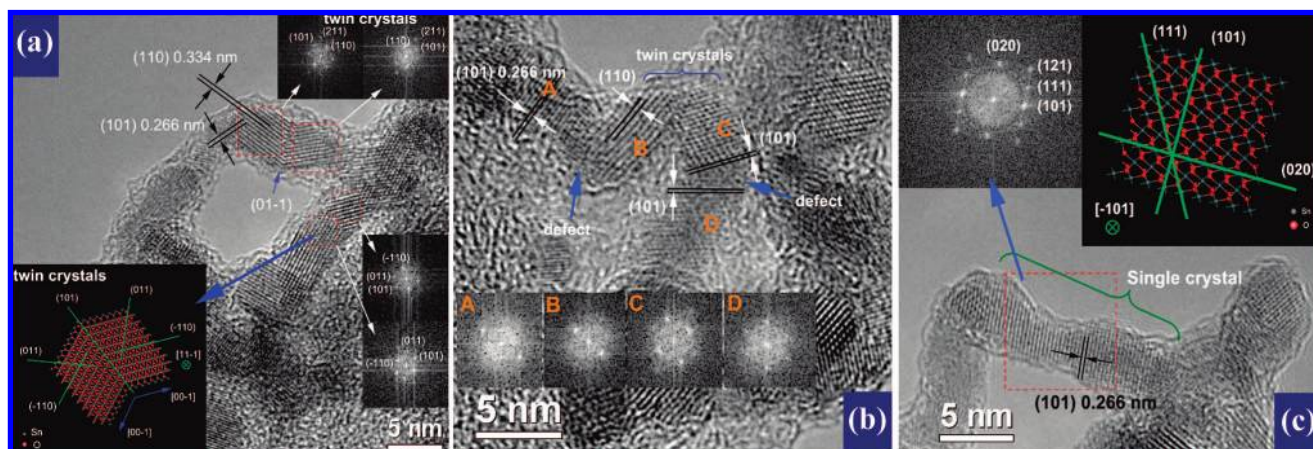

Figure 3. Attachment structures of SnO₂ ultrathin nanowires: (a) type I (twin-crystal) attachment; (b) twin crystals (B−C) and type II (plane/interface-defect) attachment (A−B and C−D); (c) type III attachment to form a single crystal.

in size/dimension. The effective particle size δ and the effective strain η are related by the following equation:[13]

$$\frac{\beta \cos \theta}{\lambda} = \frac{1}{\delta} + \eta \frac{\sin \theta}{\lambda} \qquad (1)$$

where θ is the Bragg angle of the peak, λ is the X-ray wavelength, and β is the full width at half-maximum (FWHM) in radians, which can be estimated from the expression

$$\beta = \frac{\beta_{1/2} - \beta_{p}}{0.89} \qquad (2)$$

where $\beta_{1/2}$ and β_{p} are the FWHMs obtained for nanocrystals and micron-sized powders, respectively. Values of $\beta_{1/2}$ were extracted from XRD patterns by Lorentzian multipeak fitting, while $\beta_{p} = 0.25$ was taken as a constant quantity. The negative slopes (η) of the linear fits to the plots of $\beta \cos \theta$ versus $\sin \theta$ indicate compressive strain (Figure 2b). The effective nanocrystal diameters (δ) were determined to be 0.8, 1.0, 1.7, 3.5, and 2.0 nm for SnO₂ *s*-QDs, QDs, NWs (4 and 18 h), and *me*-NCs, respectively. The strain η decreased from −8.4% to −1.2% as the dimension increased from 0D to 1D. The strain indicates the distortion of the nanocrystal lattice. The size-related strain

(13) (a) Hall, W. H. *Proc. Phys. Soc. London, Sect. A* **1949**, *62*, 741–743. (b) Williamson, G. K.; Hall, W. H. *Acta Metall.* **1953**, *1*, 22–31. (c) Kang, J. Y.; Tsunekawa, S.; Kasuya, A. *Appl. Surf. Sci.* **2001**, *174*, 306–309.

was also observed in sol−gel-prepared SnO₂ NCs.[13c] Besides the size-decrease-induced lattice distortion/strain, the reduced (Sn²⁺) surface, defects, and organic capping ligands also contributed. As shown in Figure 2b, the deviation from the linear relationship was mainly induced by the (101) data in SnO₂ QDs (partially attached) and NWs (4 h). It was observed by HRTEM that {101} is the most common attachment plane in SnO₂ NWs (Figure 3a and Figure SI-3 in the Supporting Information). Therefore, the deviation could be the result of extra compressive strains [i.e., increased η (abs.)] in the [101] direction induced by oriented attachment. This is further verified by the fact that for the SnO₂ *s*-QDs, for which attachment does not happen, and the NWs with the long growth/annealing time (18 h), where the strain is relaxed, this deviation becomes small (Figure 2b).

To demonstrate the formation mechanism of SnO₂ NWs, both QD and NW crystal structures were closely investigated by HRTEM. It was observed that the well-dispersed SnO₂ QDs have a high degree crystallinity and exhibit a crystal lattice with fine resolution, as shown in Figure 1a. The plane distances of (110) and (101) were estimated to be 0.334 and 0.266 nm, respectively, which are very consistent with the XRD results. The HRTEM images of SnO₂ ultrathin NWs demonstrate that the NWs are in fact composed of nanocrystals that are connected (attached) with each other in series. Furthermore, careful analysis of the junctions showed that there are three types of attachments (Figure 3 and Figure SI-3 in the Supporting Information). Type

I is twin-crystal attachment, in which crystals on both sides of the junction share a surface/interface with the same plane index. The inserted crystal structure graph (lower-left inset in Figure 3a) gives a visual interpretation of this type of attachment. A {101} plane is shared by the twin nanocrystals. Type II is plane/interface-defect attachment, that is, the attached surfaces of the two connected nanocrystals are from different crystal-plane groups. Figure 3b shows a typical type-II attachment between crystals A and B: the interface plane of crystal A is (101) and that of crystal B is (110). The type-II attachment between C and D involves a small-angle boundary, which suggests that the interface has a high index plane with step defects. The mismatch of interface lattices inevitably introduces lattice distortion and reconstruction, which induce strain in the NW. Attachment of type III is actually not an attachment in the NW state but consists of a rod-shaped single crystal (aspect ratio up to 3−5) within an NW, as shown in Figure 3c and Figure SI-3b,e in the Supporting Information. Since the SnO₂ QDs are nearly spherical in shape (Figure 1a and Figure SI-1a in the Supporting Information), it is reasonable to believe that single-crystal attachment evolves from the precise oriented attachment of separate nanocrystals. This type of attachment reduces the interface energy by the greatest amount.

Size and Surface Effects in SnO₂ QDs and NWs. PL spectra were measured for SnO₂ nanomaterials dispersed in chloroform. The absorption spectra of dodecanethiol-modified SnO₂ QDs, me-NCs, and NWs (Figure 4a) were measured in film states prepared by the dip-drying method. To extract the SnO₂ band-gap information, we used the differential function (Figure 4b), which is a convenient method for extrapolation or fitting calculations.[7g,8,14] The quantum-confinement effect was unambiguously observed as the dimension was decreased from 1D (NWs) to 0D (QDs). The band gaps were determined from the differential absorption maxima, which were measured to be 246, 272, 288, 284, and 300 nm for SnO₂ s-QDs, QDs, me-NCs, and NWs (4 and 18 h), respectively. In accord with the absorption spectra, the peaks in the PL spectra were located in the range 350−600 nm for OA−oleylamine-capped SnO₂ (Figure 4e) and 270−550 nm for dodecanethiol-exchanged SnO₂ samples (Figure 4f,g); both sets of PL spectra showed the size-dependent shift and the blue shift induced by thiol capping.

The exciton Bohr radius of SnO₂ is estimated to be 2.7 nm. Therefore, the synthesized SnO₂ QDs and me-NCs as well as the NWs in the radial dimension are in the strong-quantum-confinement regime. When the nanocrystal radius is smaller than Bohr radius, the effective band-gap energy E_g^{eff} is given by eq 3, which was derived by Brus using the effective mass approximation (EMA):[15]

$$E_g^{eff} = E_g + \frac{\hbar^2 \pi^2}{2\mu R^2} - \frac{1.8 e^2}{4\pi\varepsilon_0 \varepsilon R} + \text{smaller terms} \quad (3)$$

where E_g is the bulk band-gap energy, R is the nanocrystal radius, $\hbar$ is Planck's constant divided by 2π, and μ is the effective reduced mass. For bulk SnO₂, $\varepsilon = 14$ and $\mu \approx m_e^* = 0.275 m_e$ (because $m_e^* \ll m_h^*$, where m_e^* and m_h^* are the effective masses of the electron and hole, respectively). With R near or larger than the exciton Bohr radius, the third term on the right-

hand side of eq 3, which gives the correlation between electron and hole positions that is induced by Coulomb interaction, can be ignored. In this case (the weak-confinement regime), E_g^{eff} is simply described by the major additive effect of the independent confinement energies for the electron and the hole:

$$E_g^{eff} \approx E_g + \frac{\hbar^2 \pi^2}{2\mu R^2} \quad (4)$$

The calculated band gaps and the measured values from the absorption spectra are plotted in Figure 4c. The results indicate that the size−band-gap data for the me-NCs can be described by the strong-confinement model (eq 3), while the SnO₂ NWs (3.5 nm diameter) show a weak-confinement tendency (eq 4). Since the average radius of the SnO₂ ultrathin NWs is ∼1.75 nm (i.e., less than the exciton Bohr radius of 2.7 nm) and the NW length is much greater than the exciton Bohr radius, the band gap of 300 nm (4.13 eV) should be attributed to the diameter confinement. In the axial dimension, the electron is highly delocalized, and the confinement effect fades. The tails at ∼320−340 nm (3.88−3.65 eV) in the absorption spectra of the SnO₂ NWs are very near the bulk band gap (3.6 eV), indicating the 1D delocalization feature. This is also true for NWs of other semiconductors, e.g., CdSe. The bulk exciton Bohr radius of CdSe is 5.5 nm. For CdSe rods longer than ∼10 nm, the spectrum is strongly dependent on the diameter (which is still strongly confined) and shows little dependence on the length (which has already become a weakly confined axis).[16] InAs shows significant length-dependent effects, as its exciton Bohr radius is much larger (∼35 nm).[6] Since the exciton Bohr radius of SnO₂ is rather small, length-dependent quantum-confinement effects in this material are difficult to achieve. Figure 4c also shows that when the SnO₂ size is much smaller ($R < 0.75$ nm), the Brus EMA model deviates from the observed band gap. This failure is generally observed for ultrasmall NCs, especially for CdS, PbS, and ZnS.[17] The reason for this deviation is that the Brus equation adopts the conventional infinite-depth well model. Therefore, different models have been built in order to account for this discrepancy. One is the finite-depth well model suggested by Nosaka;[17c] Figure 4c shows the calculated result obtained using this model with a well depth of 4.5 eV and effective masses $m_e^* = 0.275 m_e$ and $m_h^* = 10 m_e^*$. The Coulomb interaction energy in eq 3 was used for approximate estimation. The result agrees well with the observed absorption band gaps of QDs and NWs (1.7 nm diameter), indicating that in such small/thin SnO₂ QDs and NWs, electrons would leak out of the QDs/NWs, thus decreasing the kinetic energy. This means that if the quadratic relation (R^2) continues to hold for ultra-small/thin QDs/NWs, the decrease in the kinetic energy corresponds to the increase in the effective mass, which cannot be introduced in the infinite-well model. Additionally, the size/morphology distribution, lattice compression, and surface condition are other factors that would influence the energy structure.

The thiol-exchange reaction was selected as a feasible strategy for investigating how the SnO₂ optical properties can be tuned by the surface-capping ligands. In a typical reaction, 0.1 g of

(14) (a) Satoh, N.; Nakashima, T.; Kamikura, K.; Yamamoto, K. *Nat. Nanotechnol.* **2008**, *3*, 106–111. (b) Dong, A.; Wang, F.; Daulton, T. L.; Buhro, W. E. *Nano Lett.* **2007**, *7*, 1308–1313.
(15) (a) Brus, L. E. *J. Chem. Phys.* **1984**, *80*, 4403–4409. (b) Brus, L. E. *J. Phys. Chem.* **1986**, *90*, 2555–2560.

(16) (a) Katz, D.; Wizansky, T.; Millo, O.; Rothenberg, E.; Mokari, T.; Banin, U. *Phys. Rev. Lett.* **2002**, *89*, 086801. (b) Li, L. S.; Hu, J. T.; Yang, W. D.; Alivisatos, A. P. *Nano Lett.* **2001**, *1*, 349–351. (c) Hu, J. T.; Wang, L. W.; Li, L. S.; Yang, W. D.; Alivisatos, A. P. *J. Phys. Chem. B* **2002**, *106*, 2447–2452.
(17) (a) Lippens, P. E.; Lannoo, M. *Phys. Rev. B* **1989**, *39*, 10935–10942. (b) Rama Krishna, M. V.; Friesner, R. A. *Phys. Rev. Lett.* **1991**, *67*, 629–632. (c) Nosaka, Y. *J. Phys. Chem.* **1991**, *95*, 5054–5058.
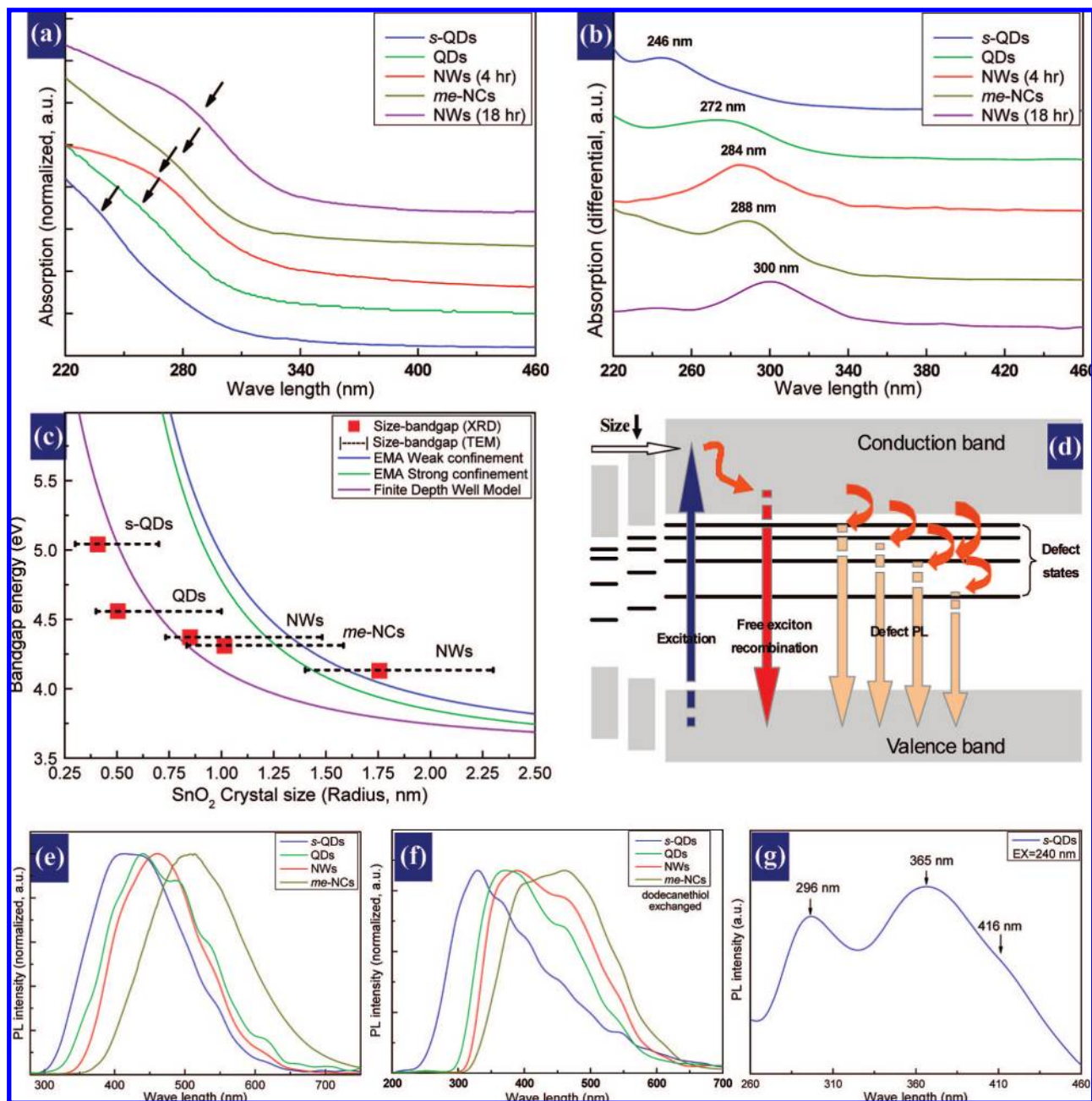
Figure 4. (a) UV–vis absorption spectra and (b) the corresponding differential absorption spectra from long to short wavelength. (c) Observed size–bandgap data and calculated results obtained using the EMA strong-confinement and weak-confinement models and the finite-depth well model. (d) Schematic illustration of the quantum-confinement effect and the PL mechanism. PL spectra of (e) SnO$_2$ nanomaterials [excitation wavelength (EX) = 250 nm] and (f) dodecanethiol-exchanged SnO$_2$ nanomaterials (EX = 250 nm for QDs, NWs, and *me*-NCs; EX = 200 nm for *s*-QDs). (g) PL spectrum of dodecanethiol-exchanged SnO$_2$ *s*-QDs (EX = 240 nm).

SnO$_2$ was dispersed in 10 mL of chloroform, after which 0.2 mL of dodecanethiol was added and the mixture kept stirring for 30 min at room temperature. Addition of ethanol and centrifugation resulted in separation of the yellowish modified SnO$_2$, which was washed again to remove residual dodecanethiol. FT-IR measurements (Figure 5a) showed that after the ligand exchange, the C=O stretching vibration at 1735.7 cm^{-1} disappeared while the N–H modes at 1618.1, 1465.7, and 1375.1 cm^{-1} remained (the peak at 1618.1 cm^{-1} may have overlapped with that of the bending vibration mode of H$_2$O). This indicated that the dodecanethiol replaced the oleic acid but had less effect on the capping oleylamine. The strong anchoring of the oleylamine suggests its templating role in the

formation of SnO$_2$ NWs. The positions of the peaks for both capping C=O and N–H groups were shifted by small amounts from those of the oleic acid and oleylamine pure liquids at 1708.7 and 1619.9 cm^{-1}, respectively, probably because of coordinate interaction. In spectra i and ii in Figure 5a, the modes in the range 2920–2850 cm^{-1} are the CH$_2$ and CH$_3$ symmetric and asymmetric stretching vibrations. Sn–O, C=O, and O–H absorptions were also observed in the Sn–OA precursor. In Figure 5, black cycle: H$_2$O or OH; green: 1700–1735 cm^{-1} of C=O stretch, 1450–1470 cm^{-1} CH$_2$ bending vibration, 1375 cm^{-1} symmetric COO^{-1} stretch; blue: 1618–1620 cm^{-1} N–H bending or H$_2$O bending, 3300–3500 cm^{-1} N–H stretch; red: Sn–O stretching modes.
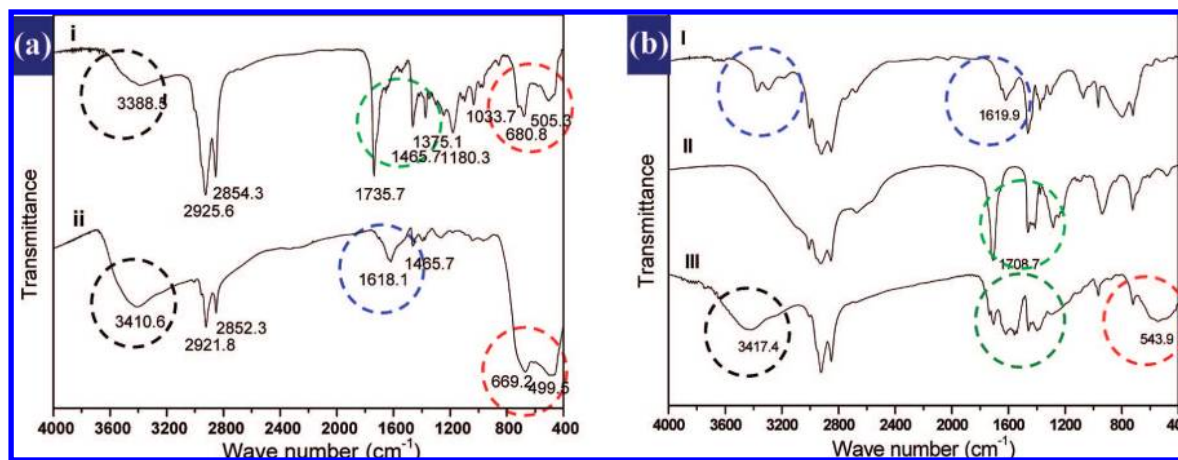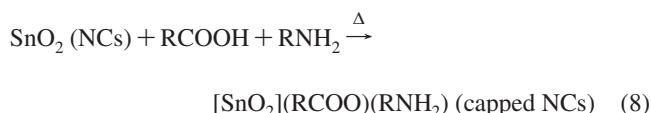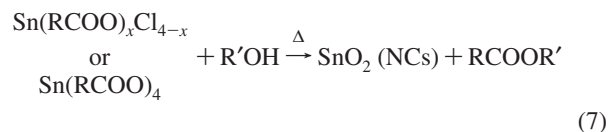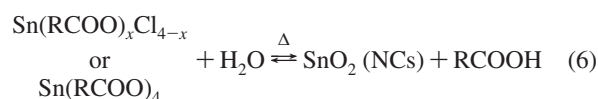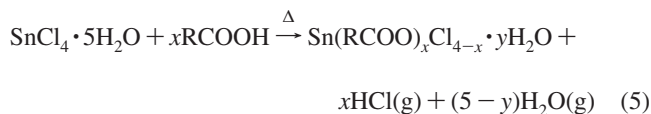
Figure 5. (a) FT-IR spectra of SnO$_2$ NWs (i) before and (ii) after dodecanethiol exchange and (b) FT-IR spectra of (I) oleylamine, (II) oleic acid, and (III) the Sn–OA precursor.

All of the PL spectra of the samples exhibited a blue shift after dodecanethiol exchange (Figure 4e–g), illustrating the possibility of band design in SnO$_2$ nanomaterials by surface modifications involving capping ligands or core–shell structures. There are several mechanisms that contribute to the observed PL spectra (Figure 4d). First, electrons are stimulated to a highly excited state in the conduction band. In a short time, the carriers relax to the band edge. Some carriers are trapped by the shallow defects in the band gap. They either recombine with holes in the valence band or continue to relax to deeper defect states before recombining. The shoulders or steps in the PL spectra of the SnO$_2$ QDs and NWs in the visible range can be interpreted by this mechanism. Those defect states are generally oxygen vacancies that are likely to form in SnO$_2$ surface.[8,18] The other mechanism is that under certain conditions, free-exciton recombination happens through a band-edge emission without capture of the excitons by the trap states. The size-induced PL shift can be explained by the quantum-confinement effect, which widens the band gap. Dodecanethiol exchange most probably increases the recombination rate of both the defect states and the free excitons. Therefore, on one hand, it induces a blue shift for all of the samples because of the enhanced prior recombination of the shallow states compared with the deeper ones. On the other hand, when excitation is just above the band edge, the relaxation within the conduction band is limited; thus, the band edge can be saturated with free excitons, thereby facilitating the free-exciton emission. Figure 4g shows such an example: when dodecanethiol-modified SnO$_2$ *s*-QDs were excited at 240 nm, corresponding to the band-gap energy of 5.2 eV, ultraviolet PL emissions at 296 and 365 nm were observed; the 296 nm peak is due to a typical free-exciton recombination (4.2 eV) and the peak at 365 nm to defect PL (3.4 eV). A higher excitation energy (200 nm, 6.2 eV) can only induce a mixture PL emission (Figure 4f), which again indicates the relatively low free-exciton recombination rate and the high rate of relaxation from conduction-band to defect states. As expected, dodecanethiol-modified SnO$_2$ NWs lead to similar PL behavior. Figure SI-4 in the Supporting Information shows that when the excitation wavelength approached the PL edge from the short-wavelength side (EX = 300 nm), the relative intensity of the first emission state at 367 nm increased compared with the side

shoulders. The defect states at 408 and 432 nm could also be clarified when the excitation wavelength was properly chosen. It was noticed that although the *me*-NCs have smaller sizes than the NWs and their absorption state has a higher energy than that of the NWs, the *me*-NC PL peak is in the long-wavelength side, indicating the importance of shape, aggregation status, and defects to optical properties. Also, the 1D structure may help the exciton coherence and giant-oscillator effect.[19]

Evolution of Morphology from QDs to NWs. As was identified by Peng and co-workers,[20] in mixed alcohol/acid systems without oleylamine, the formation reactions of nanoc-rystals of In$_2$O$_3$, ZnO, Fe$_3$O$_4$, etc., take the pathways of hydrolysis and esterification. We suggest that the growth of SnO$_2$ QDs and NWs also proceeds by similar reactions (eqs 5–8):

$$SnCl_4 \cdot 5H_2O + xRCOOH \xrightarrow{\Delta} Sn(RCOO)_xCl_{4-x} \cdot yH_2O +$$

$$xHCl(g) + (5-y)H_2O(g) \quad (5)$$

$$\begin{matrix} Sn(RCOO)_xCl_{4-x} \\ \text{or} \\ Sn(RCOO)_4 \end{matrix} + H_2O \xrightleftharpoons{\Delta} SnO_2\,(NCs) + RCOOH \quad (6)$$

$$\begin{matrix} Sn(RCOO)_xCl_{4-x} \\ \text{or} \\ Sn(RCOO)_4 \end{matrix} + R'OH \xrightarrow{\Delta} SnO_2\,(NCs) + RCOOR'$$

$$(7)$$

$$SnO_2\,(NCs) + RCOOH + RNH_2 \xrightarrow{\Delta}$$

$$[SnO_2](RCOO)(RNH_2)\,(\text{capped NCs}) \quad (8)$$

The formation of SnO$_2$ NWs can be described as an oriented attachment,[5,21] that is, after the primary seed-incubation stage

(18) (a) Munnix, S.; Schmeits, M. *Phys. Rev. B* **1983**, *27*, 7624–7635. (b) Batzill, M.; Katsiev, K.; Burst, J. M.; Diebold, U.; Chaka, A. M.; Delley, B. *Phys. Rev. B* **2005**, *72*, 165414.

(19) Tokihiro, T.; Manabe, Y.; Hanamura, E. *Phys. Rev. B* **1993**, *47*, 2019–2030.

(20) Narayanaswamy, A.; Xu, H. F.; Pradhan, N.; Kim, M.; Peng, X. G. *J. Am. Chem. Soc.* **2006**, *128*, 10310–10319.

(21) (a) Penn, R. L.; Banfield, J. F. *Science* **1998**, *281*, 969–971. (b) Alivisatos, A. P. *Science* **2000**, *289*, 736–737. (c) Pacholski, C.; Kornowski, A.; Weller, H. *Angew. Chem., Int. Ed.* **2002**, *41*, 1188–1191. (d) Lu, W.; Gao, P.; Jian, W. B.; Wang, Z. L.; Fang, J. *J. Am. Chem. Soc.* **2004**, *126*, 14816–14821. (e) Cho, K. S.; Talapin, D. V.; Gaschler, W.; Murray, C. B. *J. Am. Chem. Soc.* **2005**, *127*, 7140–7147. (f) Ribeiro, C.; Lee, E. J. H.; Longo, E.; Leite, E. R. *ChemPhysChem* **2005**, *6*, 690–696.

within 30 min of reaction, the nanoseeds intend to attach to each other, forming QD attachments or strings. As the process continues to progress, annealing and welding of the attached nanocrystals take place, forming long, branched ultrathin NWs. A schematic description of the growth is shown in Figure 1d.

According to the general Derjaguin−Landau−Verwey−Overbeek (DLVO) theory of colloid stability, the forces between nanocrystals or colloidal particles in solution mainly include the Coulomb, charge−dipole, dipole−charge, dipole−dipole, and van der Waals interactions. Generally, semiconductor nanoparticles possess large, permanent dipole moments (41−98 D).[22] Therefore, in a unary nanocrystal system, dipole−dipole interactions may become dominant for the nanocrystal attachment behavior. The dipole−dipole energy $W_{\mu-\mu}$ between two nanoparticles can be written as[23]

$$W_{\mu-\mu}(r, \theta', \phi) = \frac{\mu_i \mu_j \cos \theta_j'}{4\pi\varepsilon_0 \varepsilon r_{ij}^3}(\cos \theta_i')(\cos \theta_j')[2 + 2kr_{ij} + (kr_{ij})^2]$$

(9)

in which r_{ij} is the distance between the centers of nanoparticles i and j, θ' and ϕ are standard angle parameters in a spherical polar coordinate system, $1/k$ is the Debye screening length, ε_0 is the dielectric constant of vacuum, ε is the effective dielectric constant of the solution layers between the two nanocrystals, and μ_i and μ_j are the dipole moments of the nanoparticles. From eq 9, when ε is relatively large, the dipole−dipole interaction is suppressed; for small ε, the dipole−dipole attraction becomes prominent. Because OA and oleylamine have relatively small dielectric constants, the alcohol species gain importance. Experiments showed that when the other reaction parameters were kept unchanged (reaction time of 18 h), choosing alcohols with larger ε [e.g., ethylene glycol ($\varepsilon = 37$), methanol ($\varepsilon = 32.6$), or glycerol ($\varepsilon = 43$) at room temperature] yielded nanocrystals while using alcohols with smaller ε [e.g., ethanol ($\varepsilon = 25$), hexanol ($\varepsilon = 13.3$), or n-butanol ($\varepsilon = 8$)] incubated SnO₂ ultrathin NWs. These results indicate that the NW growth mechanism should be a dielectric-constant-mediated attachment induced by dipole−dipole attraction. We also found that this discipline was applicable to the interpretation of some attachment morphologies of other oxide nanocrystals prepared in similar systems, e.g., In₂O₃. Meanwhile, those alcohols showed no apparent difference in the formation stage for SnO₂ QDs. The clumplike aggregation of *me*-NCs is the result of thermodynamic evolution, in consideration of the relatively large electrostatic repulsion.[23] The competition/coupling of the dipole−dipole attraction with the surface-lattice mismatch/match gives an explanation for the three types of attachments described above. Complete attachment orientations could be concluded from a careful analysis using HRTEM. Since the attachment interfaces can be categorized into three types, the attachment can be regarded as quasi-oriented or imperfectly oriented.[21a]

In addition to the dipole-induced oriented attachment mechanism, there are other two indispensable factors for the formation of NWs: the oleylamine and trace water (the crystalline water in SnCl₄·5H₂O). When oleylamine was not introduced into the system, only SnO₂ QDs were obtained. The FT-IR spectra

(Figure 5a,b) showed that both OA and oleylamine are capping ligands for the SnO₂ NWs. Since oleylamine does not take part in the reaction directly, it probably serves as a surface-selective ligand (eq 8), otherwise known as a molecular template, for SnO₂ NW formation.[24] Equations 6 and 7 show that SnO₂ can be prepared via both hydrolysis and esterification reactions. When anhydrous SnCl₄ was used, only SnO₂ QDs could be prepared; no SnO₂ NWs formed. Adding ∼1 mL of additional H₂O yielded SnO₂ NWs without apparent differences from those formed via crystalline water only. FT-IR spectra indicated that there is H₂O/OH in the precursor and SnO₂ products. The trace water is suspected to coordinate to the SnO₂ surface and thus would take part in the oriented attachment. Quantum-mechanical calculations have shown that surface water molecules may greatly enhance the polarity of semiconductor NCs.[25] Similar effects could also be expected in SnO₂, but the exact mechanism showing how oleylamine and H₂O take part in NW formation still needs further investigation.

Further examination of the attachment mechanism was carried out by a two-step preparation strategy. The SnO₂ QDs were first prepared and then redispersed into an equivalent fresh reaction solution containing no additional tin source. SnO₂ NWs were also obtained through this route. In view of the fact that the radii of the SnO₂ s-QDs to NWs increase sequentially, the nucleation, growth, and oriented-attachment processes are overlapped in the 1-step synthesis. Separation of these steps has been proved to be very important in the synthesis of monodispersed nanocrystals[26] and will provide opportunities for preparing SnO₂ NWs with more-designable morphologies.

Self-Assembled 2D and 3D Porous Structures. Self-assembled 2D patterns of SnO₂ QDs as building blocks were prepared on silicon-wafer surfaces (Figure 6a−d). These 2D porous structures generally had random, hexagonal, distorted hexagonal, or square patterns. We have discussed elsewhere the formation mechanism of such hierarchical hexagonal structures on carbon substrates.[11] Briefly, the nanocrystals follow an irreversible drying-mediated assembly process. The appearance of ordered porous patterns complies with water-droplet self-assembly mechanisms. Different models have been developed to interpret similarly formed patterns, called breath figures, in polymer films. In these models, the thermocapillary and Marangoni forces exerted on the levitated, surface-touching, or submerged droplets are responsible for the observed hexagonal order. When nanocrystal building blocks take the roles of polymers, more abundant structures are expected to emerge from the nanocrystal-related interactions and capillary, surface-tension, or kinetic effects. Colorful reflections from these 2D patterns can be observed with slightly different incident and reflection angles (Figure 6c). In fact, because the dielectric constant and lattice size of these patterns are within a proper regime, they form nanocrystal self-assembled 2D photonic crystals (PCs). This was further indicated by the absorption spectrum (Figure SI-5 in the Supporting Information) and the reflection structure (Figure SI-6b−d in the Supporting Information) of the self-assembled

(22) (a) Blanton, S. A.; Leheny, R. L.; Hines, M. A.; Guyot-Sionnest, P. *Phys. Rev. Lett.* **1997**, *79*, 865−868. (b) Rabani, E.; Hetenyi, B.; Berne, B. J. *J. Chem. Phys.* **1999**, *110*, 5355−5369. (c) Shim, M.; Guyot-Sionnest, P. *J. Chem. Phys.* **1999**, *111*, 6955−6964.

(23) Sinyagin, A. Y.; Belov, A.; Tang, Z.; Kotov, N. A. *J. Phys. Chem. B* **2006**, *110*, 7500−7507.

(24) (a) Yang, J.; Xue, C.; Yu, S. H.; Zeng, J. H.; Qian, Y. T. *Angew. Chem., Int. Ed.* **2002**, *41*, 4697−4700. (b) Xu, X. X.; Wei, W.; Qiu, X. M.; Yu, K. H.; Yu, R. B.; Si, S. M.; Xu, G. Q.; Huang, W.; Peng, B. *Nanotechnology* **2006**, *17*, 3416−3420. (c) Park, K. H.; Jang, K.; Kim, S.; Kim, H. J.; Son, S. U. *J. Am. Chem. Soc.* **2006**, *128*, 14780−14781.

(25) Rabani, E. *J. Chem. Phys.* **2001**, *115*, 1493−1497.

(26) (a) Peng, X. G.; Wickham, J.; Alivisatos, A. P. *J. Am. Chem. Soc.* **1998**, *120*, 5343−5344. (b) Talapin, D. V.; Rogach, A. L.; Haase, M.; Weller, H. *J. Phys. Chem. B* **2001**, *105*, 12278−12285.
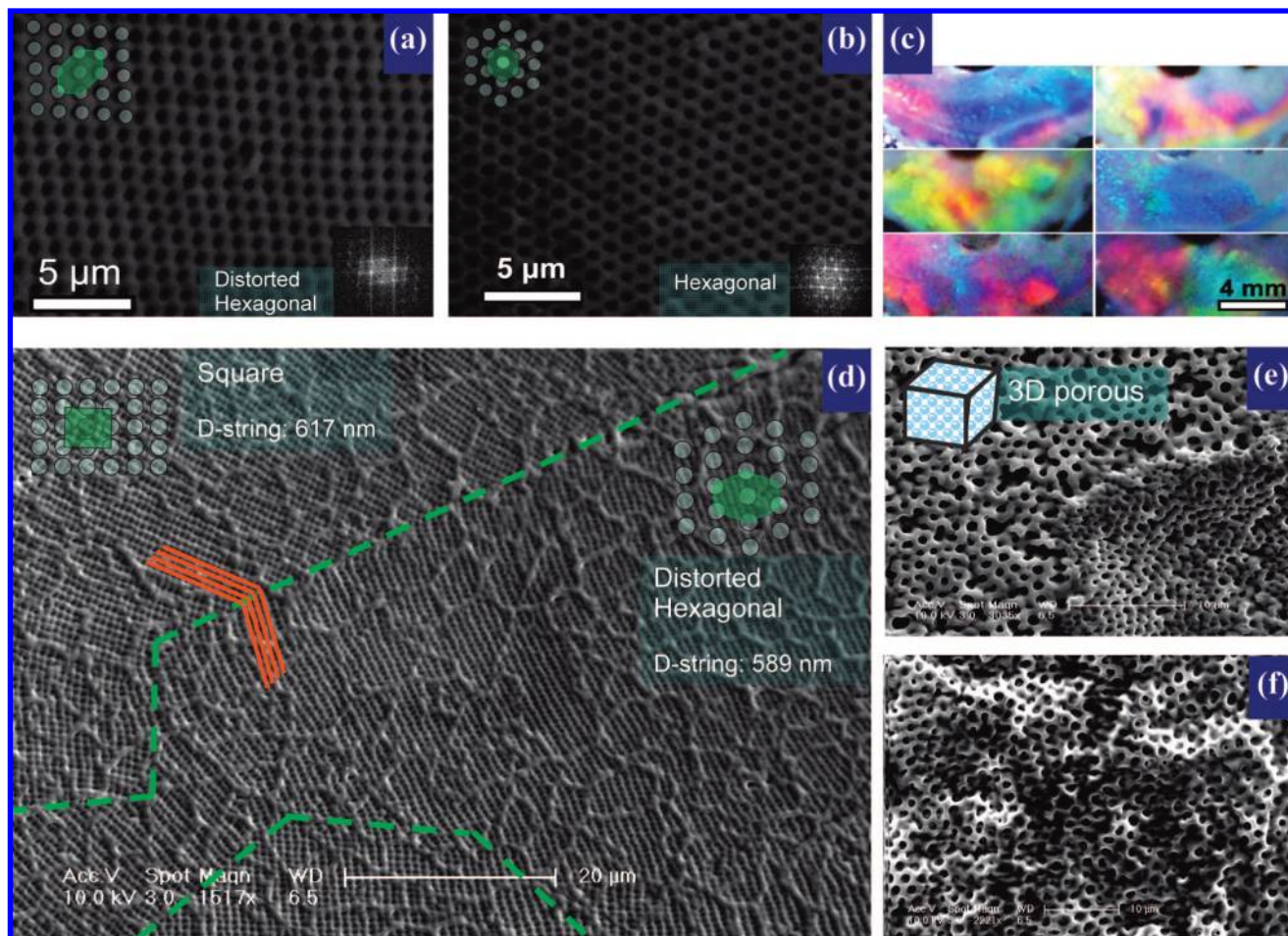
Figure 6. Self-assembled SnO₂ QDs with various patterns on silicon-wafer surfaces. (a) Distorted hexagonal pattern with (b) a coexisting hexagonal pattern. (c) Direct visual view of a fixed location with slight changes in incident and view angles. (d) Domains of square and distorted hexagonal patterns, with a rippled web surface. (e) SnO₂ QD 3D porous film structure prepared by high-humidity flow and high solution concentration. (f) Binary 3D porous film containing SnO₂ and Ag NCs.

SnO₂ QDs on a quartz-slice surface and a silicon-wafer surface, respectively.

With other parameters fixed (room temperature of 10−20 °C and SnO₂ QD concentration of 60 mg mL^{-1}), a very high relative humidity (RH > 95%) flow yielded a random porous pattern with a bigger pore size (2 μm) (Figure SI-6a in the Supporting Information); a medium-humidity (80−90% RH) flow bred a hexagonal-patterned 2D PC (0.5−1.0 μm) (Figure SI-6b−d in the Supporting Information), and a lower-humidity (60−80% RH) flow produced a mixture of hexagonal- and distorted-hexagonal-patterned 2D PCs (Figure 6a−c). When the QD concentration was increased to 120 mg mL^{-1}, the lower-humidity (60−80% RH) flow yielded domains of square and distorted hexagonal patterns together with a rippled-web surface (Figure 6d), while for in the high relative humidity (>95% RH) flow, the water droplets formed, grew, coalesced, and piled very fast, yielding a 3D porous film (Figure 6e). In the case of the 10:1 (w/w) SnO₂−Ag binary nanocrystal system, multilayered porous structures could be prepared even at the lower humidity level (60−80% RH) (Figure 6f). It was found that SnO₂ NWs were hard to form from the patterned porous structures, probably because of the size and morphology effects.[11] The distorted hexagonal pattern was occasionally noticed in polymer breath

figures, but the control factor was unclear;[27] an inclination of the substrate was reported a prerequisite.[27a] Here we have shown that in the case of QD assembly, the humidity and concentration are control factors leading to different patterns. On the basis of studies of the pattern domains in polymer breath figures, it was suggested that the domains are probably generated when two or more droplet rafts collide and incommensurately compact afterward. In our experiment, we additionally observed domains of different patterns sharing a coupled boundary: the distorted hexagonal and square patterns shown in Figure 6d both had the same value of the distance between strings (D-row = 763 nm) while the distance between adjacent pores in single strings varied (D-string = 589 nm for the distorted hexagonal pattern and 617 nm for the square pattern). Also, since the web ripple was continuous across the boundary, those pattern domains more closely resembled a phase transition than later-stage combination. Besides the capillary and Marangoni forces, consideration of nanocrystal−water-droplet interactions and the condensation/evaporation kinetics of both the water droplet and solvent are needed. In our approach, the substrate can be prepared with a level, relatively large area having a selectively controlled

(27) (a) Karthaus, O.; Cieren, X.; Maruyama, N.; Shimomura, M. *Mater. Sci. Eng., C* **1999**, *10*, 103–106. (b) Peng, J.; Han, Y. C.; Yang, Y. M.; Li, B. Y. *Polymer* **2004**, *45*, 447–452.
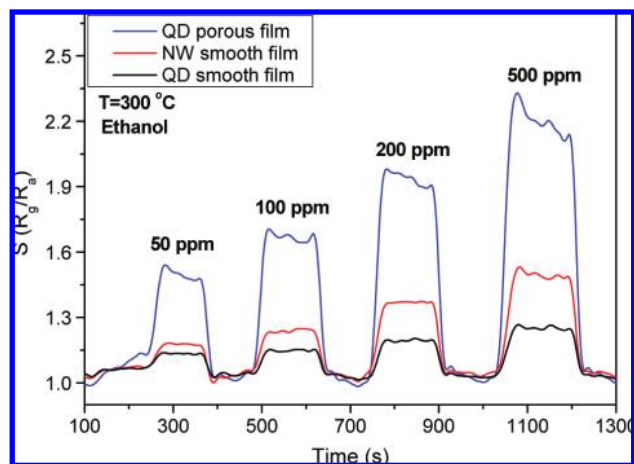
Figure 7. Gas-sensing measurements for SnO_2 QD smooth film, ultrathin NW smooth film, and QD porous film. The response and recover time is less than 20 s.

structure. This provides the opportunity for applications such as solar cells, catalysis, chemical sensing, and bioscience.

Gas-Sensing Applications. The surface states not only contribute to the structure evolution but also are important to the chemical and physical properties. By scaling down the SnO_2 nanocrystal size and designing the nanocrystal phase and morphology with different facet planes, we were able to obtain high gas sensitivity.[28] For nanocrystals synthesized via the solution system and protected by ligands, on one hand, the good solubility will aid in the formation of a smooth and condensed film, while on the other hand, this kind of gastight aggregation should be prevented in gas-sensing or catalysis applications. Li and co-workers[29] have developed a technique for preparing nanocrystal superparticles (SPs), which show mesoporous properties. Our method creates a similar nanoparticle-assembled mesoporous structure having a macroporous structure that is the reverse of the packed colloid balls. The porous films are prepared directly by a modified drying process as described above, without using any template, surfactant, or mixed solution. It is of great convenience for the coating of surfaces of various shapes and materials.

Gas-sensing measurements (Figure 7) using ethanol vapor showed that for the SnO_2 QD smooth film without porous structures, the gas sensitivity was low. The SnO_2 ultrathin NW

smooth film showed gas sensitivity that was a factor of 2 higher than the OD smooth film. Excitingly, the sensitivity of the porous film prepared from the SnO_2 QDs was nearly five times higher than that of the counterpart smooth film. At present, the sensitivity of the samples is not as high as newly reported results (R_g/R_a as large as 50.6 at 100 ppm, 300 °C).[28] The reason for this probably lies in the fact that compared with the vapor-growth method, SnO_2 measured in this paper has its surface capped with abundant oleic acid and oleylamine, which inevitably hinders its gas-sensing performance. However, the self-assembled porous structure shows exciting potential for effectiveness, and thus, our approach is a prospective method for gas-sensor fabrication. The hierarchical porous structures of binary and ternary NC systems (e.g., metal oxide) in gas sensing are under further investigation.

Conclusions

In summary, the controllable synthesis of SnO_2 quantum dots and ultrathin nanowires (quantum wires) has been achieved. The dimension evolution (0D → 1D) of the band-gap energy and PL spectra have been interpreted in terms of quantum confinement models, surface-capping ligands, and defects. Random, hexagonal, distorted hexagonal, and square 2D porous patterns (2D photonic crystals) and 3D porous structures of SnO_2 QDs have been assembled on silicon-wafer surfaces; these may find wide applications in variety of scientific fields, such as photo-electronics, catalysis, biology, etc. As an example, we have shown that this kind of hierarchically porous structure can be applied to the gas-sensing field with a significant improvement in gas sensitivity.

Supporting Information Available: HRTEM/TEM images of SnO_2 *s*-QDs and oriented attachment of ultrathin SnO_2 NWs, TEM image of *me*-NCs, PL spectra of dodecanethiol-exchanged SnO_2 NWs for different excitation wavelengths, transmission spectrum of 2D photonic crystals self-assembled by SnO_2 QDs on a quartz slice surface, and SEM images of self-assembled SnO_2 QDs with various 2D patterns on silicon-wafer surfaces. This material is available free of charge via the Internet at http://pubs.acs.org.

JA8040527

(28) Wan, Q.; Huang, J.; Xie, Z.; Wang, T. H.; Dattoli, E. N.; Lu, W. *Appl. Phys. Lett.* **2008**, *92*, 102101.

(29) (a) Wang, X.; Zhuang, J.; Huo, Z. Y.; Hu, S.; Li, Y. D. *Inorg. Chem.* **2008**, *47*, 543–547. (b) Bai, F.; Wang, D. S.; Huo, Z. Y.; Chen, W.; Liu, L. P.; Liang, X.; Chen, C.; Wang, X.; Peng, Q.; Li, Y. D. *Angew. Chem., Int. Ed.* **2007**, *46*, 6650–6653. (c) Wang, D. S.; Xie, T.; Peng, Q.; Li, Y. D. *J. Am. Chem. Soc.* **2008**, *130*, 4016–4022.